Anode-Free Lithium–Sulfur Batteries with a Rare-Earth Triflate as a Dual-Function Electrolyte Additive

Yin-Ju Yen[1] *and Arumugam Manthiram*[1,1*]

[1] Materials Science & Engineering Program and Texas Materials Institute, The University of Texas at Austin, Austin, TX 78712, USA

Corresponding Author

* E-mail: rmanth@mail.utexas.edu, manth@austin.utexas.edu (Arumugam Manthiram)

Keywords: lithium-sulfur batteries, electrolyte, metal triflate, homogeneous catalysis, polysulfide

ABSTRACT

Anode-free lithium-sulfur batteries feature a cell design with a fully-lithiated cathode and a bare current collector as an anode to control the total amount of lithium in the cell. The lithium stripping and deposition is a key factor in designing an anode-free full cell to realize a practical cell configuration. To realize effective anode protection and achieve a good performance of the anode-free full cell, the manipulation of the electrolyte chemistry toward the modification of the solid-electrolyte interphase on the anode is considered a feasible approach. In this study, the use of neodymium triflate, $Nd(OTf)_3$, as a dual-function electrolyte additive is demonstrated to promote homogeneous catalysis on the cathode conversion reactions and the anode stabilization. $Nd(OTf)_3$ not only facilitates the conversion reaction by promoting the polysulfide adsorption, but also effectively protects the lithium-metal anode and stabilizes the lithium stripping and deposition during cycling. With this electrolyte modification, both Li ‖ Li_2S half cells and Ni ‖ Li_2S anode-free full cells support a high areal capacity of 5.5 – 7.0 mA h cm^{-2} and maintain a high Coulombic efficiency of 94 – 95% during cycling.

INTRODUCTION

Lithium-sulfur batteries are emerging as one of the most potential rechargeable battery technologies with the high theoretical capacity of lithium (3,860 mA h g^{-1}) and sulfur (1,675 mA h g^{-1}) and the low material cost of sulfur ($150 per ton). To realize lithium-sulfur batteries with high energy densities for real market needs, numerous efforts have been made to optimize the cell design parameters to maximize the energy density; they include increasing the active material loading and content, decreasing the electrolyte amount, and improving the cathode utility and the anode stability.[1–5] However, in the conventional cell designs of lithium-sulfur batteries, an excess amount of lithium, which corresponds to a negative to positive electrode capacity ratio (N/P) of 20 or above, is applied to achieve stable electrochemical performance.[6,7] The excess lithium leads to an unrealistic reaction environment and thus gives an overestimation on the cell performance, which inhibits the commercialization of lithium-sulfur batteries.[7–9]

The idea of anode-free full batteries has been proposed for lithium-ion and lithium-sulfur batteries in the recent years, in which a fully-lithiated cathode is assembled with a bare non-lithium current collector as the anode to keep a limited amount of lithium in the cell during cycling.[6,10,11] With this cell configuration, there is no excess amount of lithium (N/P = 1) existing in the cell; therefore, it prevents the inflated performance from the excess lithium in the conventional lithium-metal cells, and thus provides a realistic evaluation on the cell performance to meet the practical viability.[6–11] Moreover, anode-free full cells will also eliminate the cost and complexity in handling thin lithium-metal anodes. However, since the only lithium source in the anode-free full cell comes from the fully-lithiated cathode, the efficiency of lithium stripping and deposition during the cycling process is critical for the electrochemical performance.[12,13] Effectively stabilizing the lithium stripping/deposition and improving the cyclability of lithium-metal anode become an

urgent need for anode-free full cells.[6,13] In addition, lithium sulfide (Li_2S) as the common option for the fully-lithiated cathode in anode-free lithium-sulfur cells has an ionically and electronically insulating nature, leading to a high activation barrier to overcome for the electrochemical utilization.[1,2]

Modification or reconstruction of the solid-electrolyte interphases (SEIs) on the anode has been reported as one of the most effective ways to stabilize lithium-metal anode by manipulating the chemistry of the electrolyte, since the SEI is formed by reactions between lithium metal and electrolyte in the conventional cell designs.[14–16] Rare-earth compounds, such as Nd_2O_3, have been reported to be promising for anode protection by forming an interlayer between the electrolyte and the anode.[17,18] Besides, rare-earth element doping (*e.g.* Nd^{3+} doping) has been proved to enhance the cycle stability and rate performance.[17] Specifically, rare-earth metal triflate compounds (*e.g.*, scandium triflate $Sc(OTf)_3$) initiate *in-situ* polymerization with the DOL solvent to form a quasi-solid-state electrolyte to stabilize the lithium-metal anode and improve the interfacial transport.[19] In addition, rare-earth elements in general have a low electronegativity and a high Lewis acidity to provide excellent polysulfide adsorption ability.[17,20] Therefore, rare-earth metal compounds improve the stability of lithium-sulfur batteries with some synergistic effects of lithium-ion diffusion and polysulfide adsorption.[21–25] However, rare-earth metal compounds are mostly adopted as a cathode additive,[21–25] which features heterogeneous catalysis where the catalytic polysulfide conversion mainly occurs on the surface and the catalyst is insoluble in the electrolyte.[26–28] In addition, the heterogeneous surface between catalyst and active material leads to difficulty towards fully participating in the electrochemical reactions as well as interfacial issues such as differences in the electrical conductivity.[26–28] Therefore, homogeneous catalysts are

designed to be dissolved in the electrolyte to both promote the catalytic conversion reaction and the anode stabilization.[28,29]

In this study, we present an electrolyte modification for anode-free lithium-sulfur cells with the addition of a rare-earth metal compound, neodymium triflate ($Nd(OTf)_3$), as an electrolyte additive to achieve homogeneous catalysis. The combination of neodymium ion and triflate ion is expected to show positive effects on the anode stabilization and cathode improvement. With a small concentration of $Nd(OTf)_3$ at 1.5 mM in the electrolyte, $Nd(OTf)_3$ facilitates both the cathodic conversion kinetics and the anode stabilization. Therefore, both Li ‖ Li_2S half cells and the Ni ‖ Li_2S anode-free full cells could be operated with a strict cell parameter control of a high Li_2S loading of 8 mg cm^{-2} and a low electrolyte-to-Li_2S ratio of 8 μL mg^{-1}. The good electrochemical performance in both the Li ‖ Li_2S half cells and Ni ‖ Li_2S anode-free full cells enables a high areal capacity of 5.5 – 7.0 mA h cm^{-2} and a high energy density of 12.1 – 15.4 mW h cm^{-2}.

EXPERIMENTAL SECTION

Preparation of electrolytes

The blank electrolyte was prepared with 1 M lithium bis(trifluoromethanesulfonyl)imide (LiTFSI, Sigma Aldrich) and 0.2 M lithium nitrate ($LiNO_3$, Sigma Aldrich) in a 1,3-dioxolane (DOL, Sigma Aldrich)/1,2-dimethoxyethane (DME, Sigma Aldrich) cosolvent at a volumetric ratio of 50 : 50. Neodymium trifluoromethanesulfonate ($Nd(OTf)_3$, hereafter referred to as neodymium triflate, Sigma Aldrich), as an electrolyte additive, was added into the as-prepared blank electrolyte at a concentration of 1.5 mM.

Preparation of Li_2S cathode

The lithium sulfide (Li_2S, Alfa Aesar) cathode slurry was prepared by a wet-milling method. 80 wt% Li_2S and 20 wt% carbon nanofiber (CNF) were added into a PTFE bottle and wet-ball-milled for 24 h with a roll jar-milling system (US Stoneware 802 CVM) to obtain a homogeneous slurry mixture. The mixture was then drop-cast on two commercial carbon papers as the Li_2S cathode with a diameter of 1.1 mm and dried inside the glovebox.

Materials characterization

Fourier transform infrared (FTIR) spectra were collected with a Thermo Scientific-Nicolet iS5 FTIR spectrometer. The samples for the nuclear magnetic resonance (NMR) spectroscopy analysis were prepared with a 0.1 M Li_2S_6 solution in the DME/DOL solvent, with the addition of 5 mM $Nd(OTf)_3$. Deuterated chloroform (chloroform-d) was applied as the solvent to collect the ^7Li NMR spectrum. Ultraviolet-visible (UV-vis) spectroscopy was performed with a Cary 5000 spectrometer. X-ray photoelectron spectroscopy (XPS) was conducted with a Kratos X-ray

photoelectron spectrometer with monochromatic Al Kα radiation. The obtained binding energies were calibrated with the carbon C 1s peak at 284.8 eV, and the peak fitting and data processing were performed with the CasaXPS software with a Shirley-type background. The morphology of the fresh and cycled Ni anodes was investigated with an Apero 2C Lovac scanning electron microscope (SEM). The fresh Ni anode and lithium-metal anode were collected after the first activation at the C/20 rate, and the cycled Ni anode and lithium-metal anode were collected after 20 cycles at the C/10 rate at the charged state.

Electrochemical testing

The Li || Li_2S half cells and Ni || Li_2S anode-free cells were assembled with CR2032 coin cell cases inside an argon-filled glovebox. The Li || Li_2S half cells were made with the prepared Li_2S cathode, a Celgard 2325 separator, and a lithium-metal foil as the anode. The Ni || Li_2S anode-free cells were made with a nickel foil as the anode. The Li_2S loading and the electrolyte-to-Li_2S ratio (E/Li_2S) were set, respectively, at 8 mg cm^{-2} and 8 μL mg^{-1} for the galvanostatic testing of the Li || Li_2S half cells. For the galvanostatic testing of the Ni || Li_2S anode-free cells, the Li_2S loading and the E/Li_2S ratio were set, respectively, at 4 mg cm^{-2} and 10 μL mg^{-1} or 8 mg cm^{-2} and 8 μL mg^{-1}. All the cell test data were collected with an Arbin battery testing system. Before starting the cell tests, the Li_2S cathode was activated at a C/20 rate (1C = 1,166 mA g^{-1}) by charging to 3.8 V and discharging to 1.8 V as the activation cycle. The subsequent cycling rate for the galvanostatic test was set at C/10 rate over 60 cycles for the Li || Li_2S half cells and Ni || Li_2S anode-free cells. For the lower loading condition of the Ni || Li_2S anode-free cells, the cycling rate was set at C/5 rate over 100 cycles. For the rate performance test, the Li || Li_2S half cells were cycled at C/10, C/5, C/2, and 1C rates for 5 cycles at each rate, and cycled back to C/5 for another 80 cycles.

For the electrochemical impedance spectroscopy (EIS) analysis, the impedance of the Li || Li_2S half cells was measured with an AC voltage amplitude of 5 mV in the frequency range of 1 MHz – 100 mHz at the charged state. The Li ‖ Li symmetric cell test was analyzed under a current density of 0.5 mA cm^{-2} and a capacity of 0.5 mA h cm^{-2} for 700 h, and the Li ‖ Ni asymmetric cell was cycled under a current density of 1.0 mA cm^{-2} and a capacity of 1.0 mA h cm^{-2} for 16 cycles, with an initial activation voltage to 1.0 V to strip lithium onto the Ni foil.

The rate-dependent cyclic voltammetry (CV) test was performed with the Li || Li_2S half cells on a Biologic VMP-3 system at the scanning rates of 0.050, 0.075, 0.100, and 0.125 mV s^{-1}, with each scanning rate repeated for 3 cycles. The lithium-ion diffusion coefficient was calculated from the rate-dependent CV results based on the Randles-Sevcik equation. The galvanostatic intermittent titration technique (GITT) for the Li || Li_2S half cells was performed on a Biologic VMP-3 system with an activation process at a C/20 rate to 3.8 V, followed by a discharge process to 1.8 V at a constant current of 0.466 mA for 1 h accompanied with 20 min of the relaxation time for each step. The internal resistance was determined with the ratio between the voltage difference of the closed-circuit voltage point (V_{CCV}) and the quasi-open-circuit voltage point (V_{QOCC}) to the applied current. For the temperature-dependent Li ‖ Li symmetric cell test, the EIS spectra were collected at 293, 303, 313, 323, and 333 K with an AC voltage amplitude of 5 mV in the frequency range of 1 MHz – 10 mHz. The collected spectra were fitted with a Zview software and the activation energies were calculated based on the Arrhenius equation.

Chronoamperometry for the Li_2S nucleation test

Tetraethylene glycol dimethyl ether (TEGDME) with 0.4 M Li_2S_8, 1 M LiTFSI, and 0.2 M $LiNO_3$ was applied as the catholyte, and the solution without Li_2S_8 was used as the anolyte, with

1.5 mM $Nd(OTf)_3$ as the additive in both the catholyte and anolyte. 20 μL of the catholyte was drop-cast onto a carbon-coated aluminum foil and 20 μL of the anolyte was added to the lithium-metal anode. The assembled cell was discharged at a constant current of 0.112 mA to 2.06 V, and kept at a constant voltage of 2.05 V for 70,000 s on a Biologic VMP-3 system.

Li_2S_6 symmetric cell test

0.1 M Li_2S_6 with 1 M LiTFSI in DME/DOL (volumetric ratio = 50 : 50) was prepared as the catholyte and anolyte, and 1.5 mM $Nd(OTf)_3$ was added as the additive. 20 μL of the catholyte and anolyte was drop-cast onto the carbon-coated aluminum foil as the electrodes, and the assembled cells were analyzed on a Biologic VMP-3 system with a scanning rate of 5 mV s^{-1} from -1.0 to 1.0 V.

RESULTS AND DISCUSSION

Materials characterization

Despite previous reports indicating that the triflate ions in metal triflates can induce DOL polymerization at concentrations ranging from 0.2 to 5.0 mM, leading to the formation of a quasi-solid-electrolyte,[15,16,19,30,31] the DME/DOL electrolyte with the addition of 1.5 mM $Nd(OTf)_3$ still remains as a liquid, as shown in Figure 1a. The well-dissolved $Nd(OTf)_3$ in the electrolyte and the clear electrolyte liquid indicate that the DOL polymerization might not occur at this concentration of $Nd(OTf)_3$. To further confirm the interaction between $Nd(OTf)_3$ and the DME/DOL solvent as well as the DME/DOL electrolyte, FTIR and ^7Li NMR analyses were conducted (Figure 1). From the FTIR analysis in Figure 1b, the absorbance of the DME/DOL solvent with the addition of 1.5 mM $Nd(OTf)_3$ is similar to that of pure DME/DOL solvent. No absorbance change with regard to

DOL polymerization at 850, 980, and 1150 cm^{-1} was detected in the presence of $Nd(OTf)_3$ in the FTIR spectra, indicating that there is no interaction between $Nd(OTf)_3$ and the DME/DOL solvent.[19,30,31] A similar result can be observed from the ^7Li NMR spectra of the blank DME/DOL electrolyte with and without the addition of $Nd(OTf)_3$ (Figure 1c). There is no peak shift or peak formation in the ^7Li NMR spectra, indicating that the solvation structure with the addition of $Nd(OTf)_3$ remains the same as that of the blank electrolyte. Therefore, in this study, $Nd(OTf)_3$ as an electrolyte additive does not undergo polymerization with DOL solvent at the concentration of 1.5 mM.

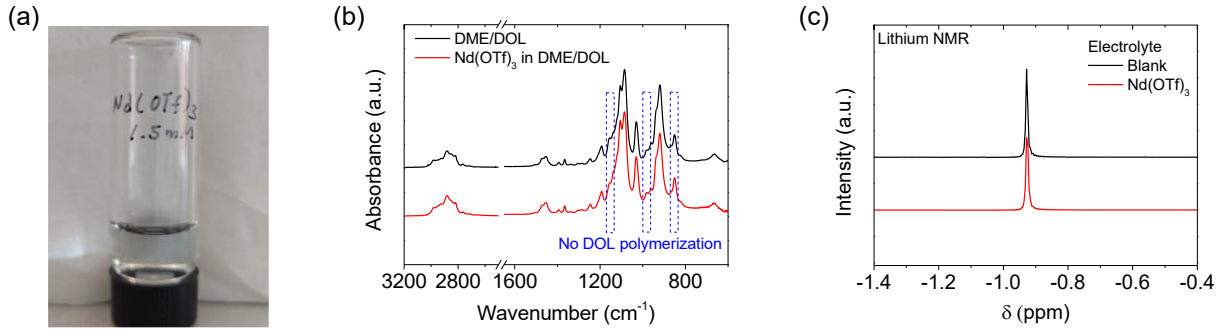

Figure 1. (a) Digital photo of the DME/DOL electrolyte with the addition of 1.5 mM $Nd(OTf)_3$, (b) FTIR spectra of the DME/DOL solvent, and (c) ^7Li NMR spectra of DME/DOL electrolyte with and without the addition of $Nd(OTf)_3$.

Cycling performances and Electrochemical analyses

To understand the effect of $Nd(OTf)_3$ as an electrolyte additive on the cycling performance, the concentration of $Nd(OTf)_3$ was first optimized (Figure S1). As seen in Figure S1, the cell with 1.5 mM $Nd(OTf)_3$ demonstrates the highest discharge capacity and the least capacity decay

throughout the cyclability test, indicating that 1.5 mM is the best concentration of $Nd(OTf)_3$ as an electrolyte additive. Therefore, we choose to apply $Nd(OTf)_3$ at the concentration of 1.5 mM as the electrolyte additive in our study. Li ‖ Li_2S half cell was employed as a lithium-excess system to explore the cathode reactivity under high Li_2S loading and lean electrolyte conditions. The corresponding first activation and the charge/discharge voltage profiles are summarized in Figures S2 and S3. During the first activation process in Figure S2, the initial activation barrier of Li_2S at ~ 3.2 V is reduced to 2.4 V with the addition of $Nd(OTf)_3$ in Li ‖ Li_2S half cell. The decrease in the activation barrier suggests that $Nd(OTf)_3$ might be helpful in intervening with the sulfur conversion reaction. From the cyclability test in Figure 2a, the Li ‖ Li_2S half cell with a Li_2S loading of 8 mg cm^{-2} and an E/Li_2S ratio of 8 μL mg^{-1} exhibits a high initial capacity of 880 mA h g^{-1} with an excellent capacity retention of 78% after 60 cycles at C/10 rate with the addition of $Nd(OTf)_3$. Besides, the average Coulombic efficiency attains 95% during cyclability test. In contrast, the capacity retention is only 48% in the control cell without $Nd(OTf)_3$ after 60 cycles, and the overall Coulombic efficiency is decreased to an average value of 89%. The voltage profile in Figure S3 depicts the typical charge/discharge plateaus of the sulfur conversion reactions;[32] however, the polarization in the control cell in Figure S3a becomes severe at the end of cycle life.

A similar trend is observed in the rate performance test, as shown in Figure 2b. As the cycling rate increases from C/10 to 1C, the difference between the discharge capacity with and without the addition of $Nd(OTf)_3$ becomes obvious. The improved rate capability with the existence of $Nd(OTf)_3$ further proves that $Nd(OTf)_3$ facilitates the sulfur conversion reactions and thus contributes to a higher discharge capacity. Therefore, in the following 80 cycles at a C/5 rate, the capacity retention with the addition of $Nd(OTf)_3$ still remains 75%, while the control half cell without $Nd(OTf)_3$ exhibits a poor capacity retention of only 32%. Besides, despite a slight decrease

in the Coulombic efficiency from 95% to 92% with the cycling process at C/5 rate, the average Coulombic efficiency with $Nd(OTf)_3$ still reaches 94% after the rate performance test. The high average Coulombic efficiency of 94% confirms the positive effects of $Nd(OTf)_3$ on catalyzing the cathode and stabilizing the lithium-metal anode, while the slight decay might be resulting from the high-loading and lean-electrolyte conditions after cycling at different higher rates. In contrast, the control cell without $Nd(OTf)_3$ fails with a dropped Coulombic efficiency of 36% at the end of the following 80 cycles due to poor cathode kinetics and anode protection. The drastic difference in the cycling performance of the Li ‖ Li_2S half cell indicates that the addition of $Nd(OTf)_3$ might effectively improve the cathodic reaction kinetics and promote lithium-metal anode stabilization in a lithium-excess condition, which is reflected on the enhanced capacity retention of 75 – 78% and the improved Coulombic efficiency of 94 – 95%.

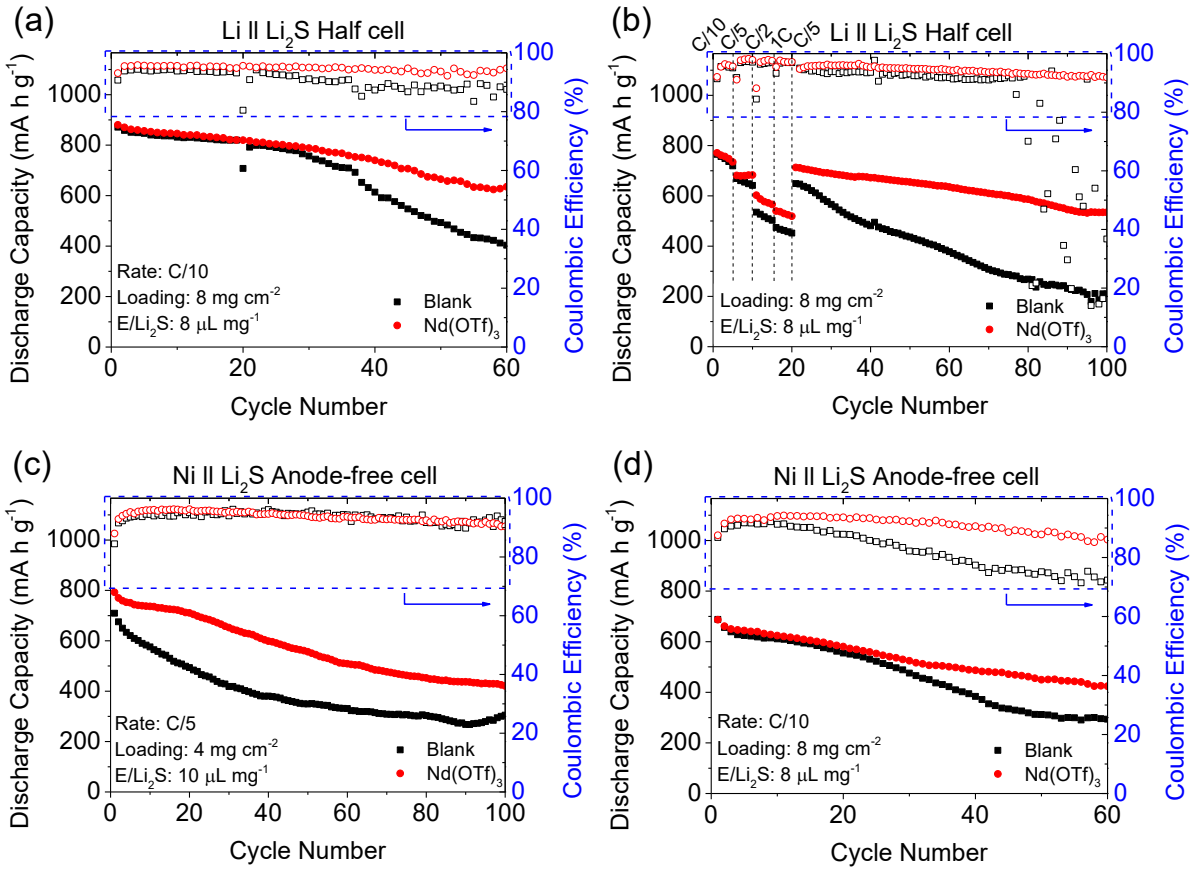

Figure 2. The cycling performance of the Li ‖ Li_2S half cell and Ni ‖ Li_2S anode-free full cell: (a) Cyclability at C/10 rate and (b) rate performance of the Li ‖ Li_2S half cell with a Li_2S loading and an E/Li_2S ratio of, respectively, 8 mg cm^{-2} and 8 μL mg^{-1}. Cyclability of the Ni ‖ Li_2S anode-free full cell (c) at C/5 rate with a Li_2S loading and an E/Li_2S ratio of, respectively, 4 mg cm^{-2} and 10 μL mg^{-1} and (d) at C/10 rate with a Li_2S loading and an E/Li_2S ratio of, respectively, 8 mg cm^{-2} and 8 μL mg^{-1}.

Since the Li ‖ Li_2S half cell is a lithium-excess system, the overall cyclability enhancement might be ascribed to the combination of the catalytic effect on the cathode and anode stabilization, with a dominant contribution from the cathode. To further investigate the impact of $Nd(OTf)_3$ on the anode, Ni ‖ Li_2S anode-free full cells were employed, which is a lithium-limited condition that

the capacity retention will be dominated by the extent of the anode degradation. With a Li_2S loading and an E/Li_2S ratio of, respectively, 4 mg cm^{-2} and 10 μL mg^{-1} in Figure 2c, the Ni ‖ Li_2S anode-free full cell with $Nd(OTf)_3$ shows a comparably higher initial discharge capacity of 793 mA h g^{-1} than the control cell without $Nd(OTf)_3$, which delivers an initial discharge capacity of 709 mA h g^{-1}. The higher initial capacity with the addition of $Nd(OTf)_3$ is attributed to the improvement in the cathode reaction kinetics. After 100 cycles at the C/5 rate, the capacity retention with $Nd(OTf)_3$ remains at 53%, while the control cell without $Nd(OTf)_3$ remains only at 43%. The inferior capacity retention without $Nd(OTf)_3$ in the lithium-limited system is resulting from an inferior stabilization of the anode.

As the Li_2S loading and the E/Li_2S ratio were further increased to 8 mg cm^{-2} and decreased to 8 μL mg^{-1}, the initial activation barrier with the addition of $Nd(OTf)_3$ in Figure S4 decreases in a similar trend as that in the Li ‖ Li_2S half cell. However, in the cyclability test at C/10 rate in Figure 2d, the cells with and without the addition of $Nd(OTf)_3$ demonstrate a similar high initial capacity of 688 mA h g^{-1}. The convergence in the initial capacity at high-loading and lean-electrolyte conditions might suggest that the cathode catalytic effect of $Nd(OTf)_3$ has not been as evident as that in the low-loading condition. However, the Coulombic efficiency of the control cell deteriorates severely from the highest value of 92% to 72% after the cycling test, while there is only a slight decay of the Coulombic efficiency from the highest value of 94% to 86% in the cell with $Nd(OTf)_3$. The obvious 20% decrease in the Coulombic efficiency with the blank electrolyte reflects the poor anode protection without $Nd(OTf)_3$ in the high-loading, lean-electrolyte, and lithium-deficient environment. Besides, the capacity retention with $Nd(OTf)_3$ still outperforms that with the blank electrolyte, which are, respectively, 62% and 42%. A lower polarization with $Nd(OTf)_3$ at the end of the cyclability test compared to the control cell is also observed in Figure

S5. The high Coulombic efficiency of an average value of 91% with $Nd(OTf)_3$ in the Ni ‖ Li_2S anode-free full cell further proves that $Nd(OTf)_3$ provides excellent lithium protection that might enable a smooth lithium stripping/deposition process during the cyclability test even in a harsh testing environment of a high Li_2S active material loading and a low E/Li_2S ratio. The results demonstrate that the addition of $Nd(OTf)_3$ both improves the cathode reaction kinetics and the anode stabilization in the Li ‖ Li_2S half cell and Ni ‖ Li_2S anode-free full cell. The dual function of $Nd(OTf)_3$ facilitates good electrochemical performance with an areal capacity of 5.5 – 7.0 mA h cm^{-2}, corresponding to a high energy density of 12.1 – 15.4 mW h cm^{-2}.

Effect of neodymium triflate on the cathode

To further explore the interaction between $Nd(OTf)_3$ and the polysulfides for facilitating the sulfur conversion reactions, polysulfide solution in DME/DOL solvent with and without $Nd(OTf)_3$ was prepared for the FTIR and NMR analyses. From the FTIR analysis in Figure 3a, there is no detection of polysulfide absorbance signals from the dried polysulfide solution with $Nd(OTf)_3$ compared to the dried blank polysulfide solution.[33] Besides, in Figure 3b, the ^7Li NMR spectrum of the polysulfide solution with $Nd(OTf)_3$ shows a negative peak shift to that of the blank polysulfide solution, indicating a solvation structure change with the presence of polysulfide and a stronger electron shielding around Li^+ with the presence of $Nd(OTf)_3$.[34] The disappearance of the absorbance signals from polysulfides in the FTIR spectrum, and the solvation structure change in the polysulfide solution in the ^7Li NMR result, both imply that there are some interactions between $Nd(OTf)_3$ and polysulfides. In the polysulfide adsorption test shown in Figure 3c, the color of the polysulfide solution with the addition of $Nd(OTf)_3$ turns clear and transparent after

resting for 24 h, and the polysulfide absorbance at 320 and 420 nm in the UV-vis spectrum decreases compared to the blank polysulfide solution.[35] The color change and the decreased absorbance with the existence of $Nd(OTf)_3$ indicates that $Nd(OTf)_3$ interacts with polysulfides via adsorption, which might be helpful in participating in the sulfur conversion reactions.

Therefore, the polysulfide solution was reacted with $Nd(OTf)_3$ and the solvent was dried to collect the remaining powder for the XPS analysis in Figure S6. As the S 2p characteristic spectra of the polysulfide powder were further investigated in Figures S6a and b, the blank polysulfide sample exhibits the typical peak positions of the polysulfide species, which correspond to the terminal sulfur (S_T^{-1}) at 161.3 and 162.5 eV, and bridging sulfur (S_B^0) at 162.8 and 164.0 eV for the $2p_{3/2}$ and $2p_{1/2}$ splitting.[36,37] However, after reacting the polysulfide with $Nd(OTf)_3$, the peak intensities of the polysulfide species S_T^{-1} and S_B^0 decrease, and a new peak labeled as Nd-S forms at 162.1 eV with its $2p_{1/2}$ splitting at 163.3 eV, which might be related to the intermediates between $Nd(OTf)_3$ and polysulfides. The formation of the sulfate species at 169.9 ($2p_{3/2}$) and 171.1 eV ($2p_{1/2}$) might result from the interaction between the DME/DOL solvent and the added triflate ion that features the sulfonate structure.[38] Besides, from the Nd 3d characteristic spectrum in Figure S6c, after reacting with the polysulfide solution, the Nd 3d spectrum shows an additional small peak at around 978.9 eV compared to that of the pure $Nd(OTf)_3$, further proving the formation of intermediates from $Nd(OTf)_3$ and polysulfides.[39] Therefore, based on these materials characterization results, $Nd(OTf)_3$ is inferred to promote the polysulfide adsorption and thus the formation of intermediates after reacting with polysulfides, which might contribute to the catalysis on the sulfur conversion kinetics.[28,29]

To further investigate the capacity boost observed in the cycling test and the catalytic effect with the addition of $Nd(OTf)_3$, polysulfide symmetric cell tests and the chronoamperometry were

conducted to examine the cathode reactivity on the liquid-to-liquid and liquid-to-solid sulfur conversion kinetics in Figures 3d–f. From the polysulfide symmetric cell result in Figure 3d, the CV curve with the addition of $Nd(OTf)_3$ shows a higher current response compared to that of the control cell without $Nd(OTf)_3$, indicating an improved liquid-to-liquid sulfur conversion kinetics with the help of $Nd(OTf)_3$. Aside from the liquid-to-liquid sulfur conversion, liquid-to-solid conversion is another critical step in sulfur conversion reactions. To evaluate the high-order polysulfide to low-order polysulfide conversion, chronoamperometry was conducted to quantify the Li_2S nucleation trend. From the chronoamperometry curves for the Li_2S nucleation study in Figures 3e and f, the cell with the $Nd(OTf)_3$ additive outperforms the control cell with a higher peak current and a larger Li_2S precipitation capacity, which are, respectively, 0.15 mA and 82.82 mA h g^{-1} with $Nd(OTf)_3$, and 0.11 mA and 53.82 mA h g^{-1} without the $Nd(OTf)_3$ additive. Both the results of the polysulfide symmetric cell and the chronoamperometry prove that the addition of $Nd(OTf)_3$ promotes the electrochemical conversion of sulfur species,[13] which accords with the enhanced discharge capacity and the capacity retention in the cycling performance mentioned before, especially in the Li ‖ Li_2S half cell where the cathodic reactivity dominates the cell performance.

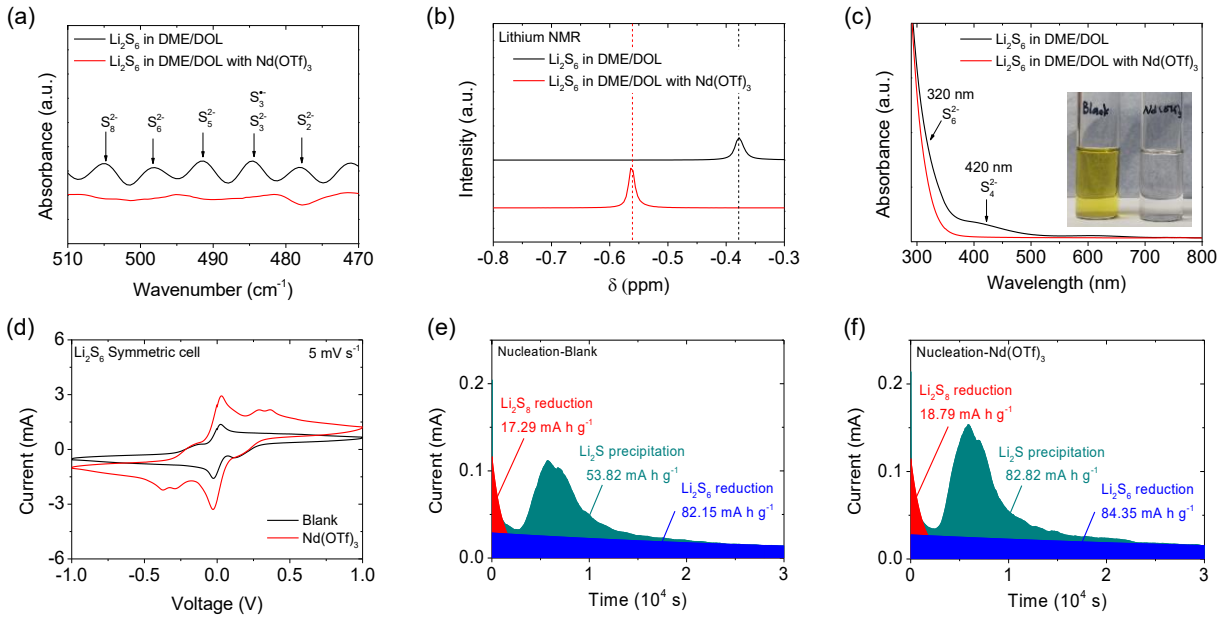

Figure 3. (a) FTIR spectra of the polysulfide solution in DME/DOL solvent, (b) ^{7}Li NMR spectra of the polysulfide solution in DME/DOL solvent, and (c) UV-vis spectra of the polysulfide solution. (d) Polysulfide symmetric cell, (e) chronoamperometry curve for the Li_2S nucleation study with the blank electrolyte, and (f) with $Nd(OTf)_3$.

To further understand the electrochemical behavior with the addition of $Nd(OTf)_3$, the impedance of the Li ‖ Li_2S half cell with and without the $Nd(OTf)_3$ additive was investigated with the EIS in Figure S7. The Nyquist plots of the fresh and cycled cells both contain two semicircles and one slope. One semicircle corresponds to the passivation layer resistance (R_{pf}) due to the formation of the SEI on the electrode in the high-frequency region, and the other semicircle corresponds to charge-transfer resistance (R_{ct}) due to the cathode lithiation/delithiation in the medium frequency region. The slope in the low-frequency region corresponds to the Warburg resistance (W_c) due to lithium-ion diffusion.[40–42] Both in the fresh and cycled conditions, the cell

with the $Nd(OTf)_3$ additive shows a lower R_{pf} than the control cell, indicating a mitigated corrosion from the polysulfide shuttle and thus an improved SEI formation.

The rate-dependent CV test was conducted to evaluate the redox reactions, as shown in Figure S8. In Figures S8a and b, both the Li ‖ Li_2S half cells with and without $Nd(OTf)_3$ exhibit four redox peaks within the working voltage window of 1.8 – 2.8 V, which are the anodic peaks of A1 and A2, and the cathodic peaks of C1 and C2. These redox peaks correspond to the oxidation of Li_2S to polysulfides and sulfur, and the reduction of the sulfur back to polysulfides and then to Li_2S.[43] The overlapped CV curves at each scanning rate are observed with and without $Nd(OTf)_3$ additive; however, the peak currents with $Nd(OTf)_3$ are higher than those with the blank electrolyte, indicating an enhanced redox reactivity with the existence of $Nd(OTf)_3$. Based on the Randles-Sevcik equation, the lithium-ion diffusion coefficient was calculated and is summarized in Table S1 and Figures S8c and d. The stronger redox peak response and the generally increased lithium-ion diffusion coefficients with the addition of $Nd(OTf)_3$ from the CV result demonstrate that $Nd(OTf)_3$ promotes the sulfur conversion and further improves the lithium-ion diffusion in the Li ‖ Li_2S half cells. In Figure S9, the activation energy for the lithium-ion diffusion is determined based on the Arrhenius equation with the temperature-dependent EIS of the Li ‖ Li symmetric cell.[44] The calculated activation energy with the $Nd(OTf)_3$ additive decreases compared to that with the blank electrolyte, which are, respectively, 57.2 and 62.9 kJ mol^{-1}. The lower activation energy indicates that $Nd(OTf)_3$ facilitates the diffusion of ions by reducing the reaction energy barrier, corresponding to the CV results. The GITT analysis in Figure S10 further provides a dynamic perspective to the effect of $Nd(OTf)_3$ on the reaction kinetics in the Li ‖ Li_2S half cell with an examination of the internal resistance.[45,46] During the first discharge process, the cell with the $Nd(OTf)_3$ additive exhibits a decreased internal resistance compared to the blank cell,

especially in the normalized time region of 15 – 30%, which corresponds to the Li_2S nucleation process. The lower internal resistance with $Nd(OTf)_3$ implies that $Nd(OTf)_3$ effectively promotes a lower energy barrier to be overcome in the sulfur conversion reactions; besides, the low resistance at the Li_2S nucleation points also indicates the facilitation of the Li_2S nucleation process, which is in agreement with the earlier cyclability test and Li_2S nucleation test results. Therefore, based on the results of the electrochemical analyses, we might infer that $Nd(OTf)_3$ has positive effects on the cathode reactions. With $Nd(OTf)_3$ as the electrolyte additive, the improvement in the sulfur conversion kinetics and the regulation of the polysulfide shuttle in the cathode mitigates the degradation of Coulombic efficiency, leading to a superior cycling performance. These benefits have been demonstrated both in the lithium-excess and lithium-limited cells.

Effect of neodymium triflate on the anode

To evaluate the effect of $Nd(OTf)_3$ in maintaining the high Coulombic efficiency in the cycling performance of the Ni ‖ Li_2S anode-free full cell, Li ‖ Li symmetric cell test and Li ‖ Ni asymmetric cell test were carried out to explore the anode stability, as shown in Figures 4a and b. From the Li ‖ Li symmetric cell test in Figure 4a, the cell with $Nd(OTf)_3$ exhibits a smooth lithium stripping and deposition with a lower overpotential for 700 h compared to that of the control cell without $Nd(OTf)_3$. The overpotential at around 500 h is 18.90 mV with $Nd(OTf)_3$, and 30.28 mV with the blank electrolyte, respectively. The Coulombic efficiency for lithium plating and stripping in the Li ‖ Ni asymmetric cell was investigated as in Figure 4b. At the end of the test, the cell with $Nd(OTf)_3$ achieves a higher Coulombic efficiency of 99.1% compared to the control cell without $Nd(OTf)_3$ (98.4%), indicating a smoother lithium stripping/deposition process with the presence

of $Nd(OTf)_3$. The low and stable overpotential for lithium stripping/deposition observed in the Li ‖ Li symmetric cell, as well as the high Coulombic efficiency in the Li ‖ Ni asymmetric cell, both indicate the positive effect of $Nd(OTf)_3$ on anode protection,[38] which promotes a smooth lithium stripping and deposition, Coulombic efficiency, and excellent capacity retention, especially with the Ni ‖ Li_2S anode-free full cell.

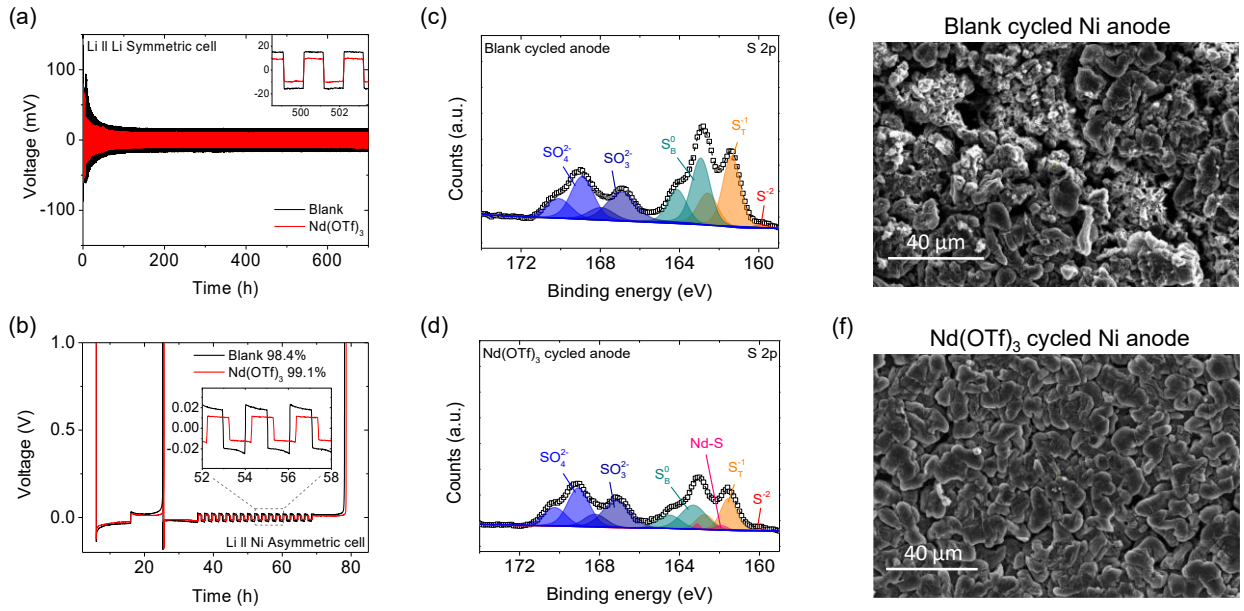

Figure 4. (a) Li ‖ Li symmetric cell and (b) Li ‖ Ni asymmetric cell. XPS S 2p spectra of the cycled Ni anodes with (c) blank electrolyte and (d) with $Nd(OTf)_3$. SEM images of the Ni foil collected from the cycled Ni ‖ Li_2S anode-free full cell with (e) blank electrolyte and (f) with $Nd(OTf)_3$.

To further explore the mechanism of $Nd(OTf)_3$ in promoting the sulfur redox reactions and the anode protection, the XPS analysis of the cycled Ni anodes retrieved from the Ni ‖ Li_2S anode-free full cell was carried out as in Figures 4c and d. From the XPS S 2p analysis, both the cycled anodes with the blank electrolyte and with the addition of $Nd(OTf)_3$ show the presence of the sulfur species, including the polysulfide S_T^{-1} and S_B^0 formed during the cycling process, and the sulfide

(S^{2-}) at 159.9 eV resulting from the reduction of polysulfide to Li_2S.[38] The formation of the sulfites (SO_3^{2-}) and sulfate (SO_4^{2-}) peaks resulting from the side reactions of lithium salts with the electrolyte is also observed at 166.9 eV and 168.9 eV as the $S2p_{3/2}$ peaks, along with their $S2p_{1/2}$ peak splitting at 168.0 and 170.1 eV, respectively.[47] However, the overall intensity ratio of the sulfide/sulfate species on the cycled anode with $Nd(OTf)_3$ is decreased compared to that of the blank anode, while the formation of the Nd-S peak still occurs at the similar binding energies at 161.9 eV ($S2p_{3/2}$) and 163.3 eV ($S2p_{1/2}$) as those observed in the polysulfide powder (Figure S6b). The similar trends in the S 2p characteristic spectra both in the dried polysulfide powder and the cycled Ni anode, as well as the Nd 3d spectra, all indicate that Nd interacts with the sulfur species and thus promotes the formation of the Nd-S SEI layer during the cycling process.[39]

For a comparison of lithium deposition, the SEM images were collected with the fresh and cycled Ni anode retrieved from the Ni ‖ Li_2S anode-free full cell (Figures 4e, f, and S11). Besides, the SEM images of the fresh and cycled lithium-anode retrieved from the Li ‖ Li_2S half cell are summarized in Figure S12 as a reference. In Figure S11, the surface morphology of the deposited lithium on the fresh Ni foil after the first activation shows a compact appearance with the addition of $Nd(OTf)_3$, while the blank Ni foil shows a porous surface with small grains distributed. After cycling at C/10 rate for 20 cycles, the lithium deposition remains uniform and dense with the $Nd(OTf)_3$ additive; in contrast, the morphology becomes nonuniform with irregular particles scattered on the surface with the blank electrolyte, as shown in Figures 4e and f. A similar trend in the surface morphology was observed in the fresh and cycled lithium-metal anodes collected from the Li ‖ Li_2S half cell. The above XPS and SEM results further correspond to the previous characterization results that $Nd(OTf)_3$ serves as a homogeneous catalyst in the electrolyte to facilitate the redox reactions in the cathode with the formation of intermediates with polysulfides.

In the meantime, it stabilizes the lithium stripping/deposition to maintain a high Coulombic efficiency and protect the anode with the formation of a Nd-S SEI layer. These bi-functional improvements in both the anode and cathode contribute to the superior cycling performance in the anode-free Li_2S full cells, which are comparative to the recent studies summarized in Table S2.

CONCLUSIONS

We presented the use of $Nd(OTf)_3$ as an electrolyte additive in both the Li ‖ Li_2S half cell and Ni ‖ Li_2S anode-free full cell. The $Nd(OTf)_3$ additive not only facilitates the cathode conversion reactions, but also stabilizes the lithium-metal anode and promotes a smooth lithium stripping and deposition process. $Nd(OTf)_3$ serving as a homogeneous catalyst effectively regulates the polysulfide migration with adsorption and forms intermediates with polysulfides, contributing to an improved cycling retention of 78% and 62%, respectively, in half cell and anode-free full cell. Besides, it protects lithium-metal anode and thus contributes to a high Coulombic efficiency of 94 – 95% throughout the cyclability test and the rate performance test. The good electrochemical performance facilitates a high areal capacity of 5.5 – 7.0 mA h cm^{-2} and a high energy density of 12.1 – 15.4 mW h cm^{-2} under strict cell operating parameters of a high Li_2S loading and a low E/Li_2S ratio of, respectively, 8 mg cm^{-2} and 8 μL mg^{-1}.

ASSOCIATED CONTENT

Supporting Information. The supporting information provides supporting figures of additive concentration optimization, charge/discharge profiles, XPS analysis, Nyquist plots of the Li ‖ Li_2S half cell, rate-dependent CV analysis, calculation of the lithium-ion diffusion coefficient,

temperature-dependent EIS of Li ‖ Li symmetric cells, GITT analysis of Li ‖ Li_2S half cell, and SEM images of fresh Ni foils, fresh lithium-metal anodes, and cycled lithium-metal anodes.

AUTHOR INFORMATION

The authors declare no competing financial interest.

ACKNOWLEDGMENT

This work was supported by the National Science Foundation, Division of Chemical, Bioengineering, Environmental, and Transport Systems, under award number 2011415. The authors would like to thank Dr. Hugo Celio, Hyunki Sul, Kameron Liao, and Tianxing Lai for assistance with XPS and insightful discussions on experimentation.

REFERENCES

(1) Manthiram, A.; Fu, Y.; Chung, S.-H.; Zu, C.; Su, Y.-S. Rechargeable Lithium–Sulfur Batteries. *Chem. Rev.* **2014**, *114* (23), 11751–11787. https://doi.org/10.1021/cr500062v.

(2) Chung, S.-H.; Chang, C.-H.; Manthiram, A. Progress on the Critical Parameters for Lithium–Sulfur Batteries to be Practically Viable. *Adv. Func. Mater.* **2018**, *28* (28), 1801188. https://doi.org/10.1002/adfm.201801188.

(3) Manthiram, A. A Reflection on Lithium-Ion Battery Cathode Chemistry. *Nat. Commun.* **2020**, *11* (1), 1550. https://doi.org/10.1038/s41467-020-15355-0.

(4) Bhargav, A.; He, J.; Gupta, A.; Manthiram, A. Lithium-Sulfur Batteries: Attaining the Critical Metrics. *Joule* **2020**, *4* (2), 285–291. https://doi.org/10.1016/j.joule.2019.12.009.

(5) Guo, W.; Zhang, W.; Si, Y.; Wang, D.; Fu, Y.; Manthiram, A. Artificial Dual Solid-Electrolyte Interfaces Based on In Situ Organothiol Transformation in Lithium Sulfur Battery. *Nat. Commun.* **2021**, *12* (1), 3031. https://doi.org/10.1038/s41467-021-23155-3.

(6) Nanda, S.; Gupta, A.; Manthiram, A. Anode-Free Full Cells: A Pathway to High-Energy Density Lithium-Metal Batteries. *Adv. Energy Mater.* **2021**, *11* (2), 2000804. https://doi.org/10.1002/aenm.202000804.

(7) Nanda, S.; Bhargav, A.; Manthiram, A. Anode-Free, Lean-Electrolyte Lithium-Sulfur Batteries Enabled by Tellurium-Stabilized Lithium Deposition. *Joule* **2020**, *4* (5), 1121–1135. https://doi.org/10.1016/j.joule.2020.03.020.

(8) Cheng, X.-B.; Yan, C.; Huang, J.-Q.; Li, P.; Zhu, L.; Zhao, L.; Zhang, Y.; Zhu, W.; Yang, S.-T.; Zhang, Q. The Gap Between Long Lifespan Li-S Coin and Pouch Cells: The Importance of Lithium Metal Anode Protection. *Energy Storage Mater.* **2017**, *6*, 18–25. https://doi.org/10.1016/j.ensm.2016.09.003.

(9) Hagen, M.; Fanz, P.; Tübke, J. Cell Energy Density and Electrolyte/Sulfur Ratio in Li–S Cells. *J. Power Sources* **2014**, *264*, 30–34. https://doi.org/10.1016/j.jpowsour.2014.04.018.

(10) Qian, J.; Adams, B. D.; Zheng, J.; Xu, W.; Henderson, W. A.; Wang, J. Anode-Free Rechargeable Lithium Metal Batteries. *Adv. Funct. Mater.* **2016**, *26* (39), 7094–7102. https://doi.org/10.1002/adfm.201602353.

(11) Nanda, S.; Gupta, A.; Manthiram, A. A Lithium–Sulfur Cell Based on Reversible Lithium Deposition from a Li_2S Cathode Host onto a Hostless-Anode Substrate. *Adv. Energy Mater.* **2018**, *8* (25), 1801556. https://doi.org/10.1002/aenm.201801556.

(12) Jung, Y.; Park, S.; Kim, J. K.; Kim, M.; Kang, B. Toward Achieving High Kinetics in Anodeless Li_2S Battery: Surface Modification of Cu Current Collector. *Adv. Funct. Mater.* **2022**, *32* (8), 2109759. https://doi.org/10.1002/adfm.202109759.

(13) He, J.; Bhargav, A.; Manthiram, A. High-Performance Anode-Free Li–S Batteries with an Integrated Li_2S–Electrocatalyst Cathode. *ACS Energy Lett.* **2022**, *7* (2), 583–590. https://doi.org/10.1021/acsenergylett.1c02569.

(14) Zhao, Y.; Ye, Y.; Wu, F.; Li, Y.; Li, L.; Chen, R. Anode Interface Engineering and Architecture Design for High-Performance Lithium–Sulfur Batteries. *Adv. Mater.* **2019**, *31* (12), 1806532. https://doi.org/10.1002/adma.201806532.

(15) Zhang, W.; Shen, Z.; Li, S.; Fan, L.; Wang, X.; Chen, F.; Zang, X.; Wu, T.; Ma, F.; Lu, Y. Engineering Wavy-Nanostructured Anode Interphases with Fast Ion Transfer Kinetics: Toward Practical Li-Metal Full Batteries. *Adv. Funct. Mater.* **2020**, *30* (39), 2003800. https://doi.org/10.1002/adfm.202003800.

(16) Jiang, C.; Ma, C.; Yang, F.; Cai, X.; Liu, Y.; Tao, X. Materials Chemistry among the Artificial Solid Electrolyte Interphases of Metallic Lithium Anodes. *Mater. Chem. Front.* **2021**, *5* (14),

5194–5210. https://doi.org/10.1039/D1QM00352F.

(17) Zhao, H.; Xia, J.; Yin, D.; Luo, M.; Yan, C.; Du, Y. Rare Earth Incorporated Electrode Materials for Advanced Energy Storage. *Coord. Chem. Rev.* **2019**, *390*, 32–49. https://doi.org/10.1016/j.ccr.2019.03.011.

(18) Snydacker, D. H.; Hegde, V. I.; Wolverton, C. Electrochemically Stable Coating Materials for Li, Na, and Mg Metal Anodes in Durable High Energy Batteries. *J. Electrochem. Soc.* **2017**, *164* (14), A3582. http://dx.doi.org/10.1149/2.0371714jes.

(19) Yang, G.; Zhai, Y.; Yao, J.; Song, S.; Lin, L.; Tang, W.; Wen, Z.; Hu, N.; Lu, L. Synthesis and Properties of Poly (1, 3-dioxolane) In Situ Quasi-solid-state Electrolytes via a Rare-Earth Triflate Catalyst. *Chem. Commun.* **2021**, *57* (64), 7934–7937. https://doi.org/10.1039/D1CC02916A.

(20) Ye, J. C.; Chen, J. J.; Yuan, R. M.; Deng, D. R.; Zheng, M. S.; Cronin, L.; Dong, Q. F. Strategies to Explore and Develop Reversible Redox Reactions of Li–S in Electrode Architectures Using Silver-Polyoxometalate Clusters. *J. Am. Chem. Soc.* **2018**, *140* (8), 3134–3138. https://doi.org/10.1021/jacs.8b00411.

(21) Ding, Z.; Li, X.; Zhang, P.; Yu, J.; Hua, Y. Enhanced Electrochemical Performance of Sulfur on Y_2O_3-Modified Porous Carbon Aerogels for High Performance Lithium–Sulfur Batteries. *New J. Chem.* **2017**, *41* (21), 12726–12735. https://doi.org/10.1039/C7NJ02714A.

(22) Li, X.; Ding, Z.; Zhang, L.; Tang, R.; He, Y. Enhanced Performance of Lithium Sulfur Batteries with Sulfur Embedded in Sm_2O_3-Doped Carbon Aerogel as Cathode Material. *Electrochim. Acta* **2017**, *241*, 197–207. https://doi.org/10.1016/j.electacta.2017.04.156.

(23) Sun, F.; Wang, J.; Long, D.; Qiao, W.; Ling, L.; Lv, C.; Cai, R. A High-Rate Lithium–Sulfur Battery Assisted by Nitrogen-Enriched Mesoporous Carbons Decorated with Ultrafine La_2O_3

Nanoparticles. *J. Mater. Chem. A* **2013**, *1* (42), 13283–13289. https://doi.org/10.1039/C3TA12846F.

(24) Li, X.; Zhang, L.; Ding, Z.; He, Y. Ultrafine Nd_2O_3 Nanoparticles Doped Carbon Aerogel to Immobilize Sulfur for High Performance Lithium–Sulfur Batteries. *J. Electroanal. Chem.* **2017**, *799*, 617–624. https://doi.org/10.1016/j.jelechem.2017.04.060.

(25) Hao, Z.; Zeng, R.; Yuan, L.; Bing, Q.; Liu, J.; Xiang, J.; Huang, Y. Perovskite $La_{0.6}Sr_{0.4}CoO_{3-\delta}$ as a New Polysulfide Immobilizer for High-Energy Lithium-Sulfur Batteries. *Nano Energy* **2017**, *40*, 360–368. https://doi.org/10.1016/j.nanoen.2017.08.039.

(26) Zhou, T.; Lv, W.; Li, J.; Zhou, G.; Zhao, Y.; Fan, S.; Liu, B.; Li, B.; Kang, F.; Yang, Q. H. Twinborn TiO_2–TiN Heterostructures Enabling Smooth Trapping–Diffusion–Conversion of Polysulfides towards Ultralong Life Lithium–Sulfur Batteries. *Energy Environ. Sci.* **2017**, *10* (7), 1694–1703. https://doi.org/10.1039/C7EE01430A.

(27) Li, Y.; Wu, J.; Zhang, B.; Wang, W.; Zhang, G.; Seh, Z. W.; Zhang N.; Sun, J.; Huang, L.; Jiang, J.; Zhou, J.; Sun, Y. Fast Conversion and Controlled Deposition of Lithium (poly) Sulfides in Lithium-Sulfur Batteries Using High-Loading Cobalt Single Atoms. *Energy Storage Mater.* **2020**, *30*, 250–259. https://doi.org/10.1016/j.ensm.2020.05.022.

(28) Luo, C.; Liang, X.; Sun, Y.; Lv, W.; Sun, Y.; Lu, Z.; Hua, W.; Yang, H.; Wang, R.; Yan, C.; Li, J.; Wan, Y.; Yang, Q. H. An Organic Nickel Salt-Based Electrolyte Additive Boosts Homogeneous Catalysis for Lithium-Sulfur Batteries. *Energy Storage Mater.* **2020**, *33*, 290–297. https://doi.org/10.1016/j.ensm.2020.08.033.

(29) Asl, H. Y.; Bhargav, A.; Manthiram, A. Taming Polysulfides in Sulfur-Based Batteries via Electrolyte-Soluble Thiomolybdate Additives. *J. Mater. Chem. A* **2020**, *10* (34), 17572–17585. https://doi.org/10.1039/D2TA03893E.

(30) Li, Z.; Tang, W.; Deng, Y.; Zhou, M.; Wang, X.; Liu, R.; Wang, C. A. Enabling Highly Stable Lithium Metal Batteries by Using Dual-Function Additive Catalyzed In-Built Quasi-Solid-State Polymer Electrolytes. *J. Mater. Chem. A* **2022**, *10* (43), 23047–23057. https://doi.org/10.1039/D2TA06153H.

(31) Zhao, Q.; Liu, X.; Stalin, S.; Khan, K.; Archer, L. A. Solid-State Polymer Electrolytes with In-Built Fast Interfacial Transport for Secondary Lithium Batteries. *Nat. Energy* **2019**, *4* (5), 365–373. https://doi.org/10.1038/s41560-019-0349-7.

(32) Yen, Y.-J.; Chung, S.-H. Lithium–Sulfur Cells with a Sulfide Solid Electrolyte/Polysulfide Cathode Interface. *J. Mater. Chem. A* **2023**, *11* (9), 4519–4526. https://doi.org/10.1039/D2TA07806F.

(33) Dillard, C.; Singh, A.; Kalra, V. Polysulfide Speciation and Electrolyte Interactions in Lithium–Sulfur Batteries with In Situ Infrared Spectroelectrochemistry. *J. Phys. Chem. C* **2018**, *122* (32), 18195–18203. https://doi.org/10.1021/acs.jpcc.8b02506.

(34) Dorai, A.; Kawamura, J.; Omata, T. Visualization of Polysulfide Dissolution in Lithium-Sulfur Batteries Using In-situ NMR Microimaging. *Electrochem. Commun.* **2022**, *141*, 107360. https://doi.org/10.1016/j.elecom.2022.107360.

(35) Liao, K.; Bhargav, A.; Manthiram, A. Scalable Metal Phosphides as a Dual-Function Catalyst and Lithium–Metal Stabilizer for Lithium–Sulfur Batteries. *ACS Appl. Energy Mater.* **2023**, *6* (18), 9585–9593. https://doi.org/10.1021/acsaem.3c01606.

(36) Wang, L.; Li, G. R.; Liu, S.; Gao, X. P. Hollow Molybdate Microspheres as Catalytic Hosts for Enhancing the Electrochemical Performance of Sulfur Cathode under High Sulfur Loading and Lean Electrolyte. *Adv. Funct. Mater.* **2021**, *31* (18), 2010693. https://doi.org/10.1002/adfm.202010693.

(37) Lai, T.; Bhargav, A.; Manthiram, A. Lithium Tritelluride as an Electrolyte Additive for Stabilizing Lithium Deposition and Enhancing Sulfur Utilization in Anode-Free Lithium–Sulfur Batteries. *Adv. Funct. Mater.* **2023**, *33* (43), 2304568. https://doi.org/10.1002/adfm.202304568.

(38) Yin, F.; Ren, J.; Zhang, Y.; Tan, T.; Chen, Z. A PPy/ZnO Functional Interlayer to Enhance Electrochemical Performance of Lithium/Sulfur Batteries. *Nanoscale Res. Lett.* **2018**, *13*, 1–7. https://doi.org/10.1186/s11671-018-2724-x.

(39) Liu, S.; Li, G. R.; Gao, X. P. Lanthanum Nitrate as Electrolyte Additive to Stabilize the Surface Morphology of Lithium Anode for Lithium–Sulfur Battery. *ACS Appl. Mater. Interfaces* **2016**, *8* (12), 7783–7789. https://doi.org/10.1021/acsami.5b12231.

(40) Song, Y. W.; Peng, Y. Q.; Zhao, M.; Lu, Y.; Liu, J. N.; Li, B. Q.; Zhang, Q. Understanding the Impedance Response of Lithium Polysulfide Symmetric Cells. *Small Sci.* **2021**, *1* (11), 2100042. https://doi.org/10.1002/smsc.202100042.

(41) Carbone, L.; Verrelli, R.; Gobet, M.; Peng, J.; Devany, M.; Scrosati, B.; Greenbaum, S.; Hassoun, J. Insight on the Li_2S Electrochemical Process in a Composite Configuration Electrode. *New J. Chem.* **2016**, *40* (3), 2935–2943. https://doi.org/10.1039/C5NJ03402G.

(42) Wang, Z.; Feng, M.; Sun, H.; Li, G.; Fu, Q.; Li, H.; Liu, J.; Sun, L.; Mauger, A.; Julien, C. M.; Xie, H.; Chen, Z. Constructing Metal-Free and Cost-Effective Multifunctional Separator for High-Performance Lithium-Sulfur Batteries. *Nano Energy* **2019**, *59*, 390–398. https://doi.org/10.1016/j.nanoen.2019.02.029.

(43) Yen, Y.-J.; Chung, S.-H. A Li_2S-Based Catholyte/Solid-State-Electrolyte Composite for Electrochemically Stable Lithium–Sulfur Batteries. *ACS Appl. Mater. Interfaces* **2021**, *13* (49), 58712–58722. https://doi.org/10.1021/acsami.1c18871.

(44) Keefe, A. S.; Buteau, S.; Hill, I. G.; Dahn, J. R. Temperature Dependent EIS Studies Separating Charge Transfer Impedance from Contact Impedance in Lithium-Ion Symmetric Cells. *J. Electrochem. Soc.* **2019**, *166* (14), A3272–A3279. http://dx.doi.org/10.1149/2.0541914jes.

(45) Park, J.; Kim, E. T.; Kim, C.; Pyun, J.; Jang, H. S.; Shin, J.; Choi, J. W.; Char, K.; Sung, Y. E. The Importance of Confined Sulfur Nanodomains and Adjoining Electron Conductive Pathways in Subreaction Regimes of Li-S Batteries. *Adv. Energy Mater.* **2017**, *7* (19), 1700074. https://doi.org/10.1002/aenm.201700074.

(46) Li, C.; Qi, S.; Zhu, L.; Zhao, Y.; Huang, R.; He, Y.; Ge, W.; Liu, X.; Zhao, M.; Xu, L.; Qian, Y. Regulating Polysulfide Intermediates by Ultrathin Co-Bi Nanosheet Electrocatalyst in Lithium−Sulfur Batteries. *Nano Today* **2021**, *40*, 101246. https://doi.org/10.1016/j.nantod.2021.101246.

(47) Nandasiri, M. I.; Camacho-Forero, L. E.; Schwarz, A. M.; Shutthanandan, V.; Thevuthasan, S.; Balbuena, P. B.; Mueller, K. T.; Murugesan, V. In Situ Chemical Imaging of Solid-Electrolyte Interphase Layer Evolution in Li–S Batteries. *Chem. Mater.* **2017**, *29* (11), 4728–4737. https://doi.org/10.1021/acs.chemmater.7b00374.

TOC Figure